IOP PUBLISHING JOURNAL OF PHYSICS D: APPLIED PHYSICS
J. Phys. D: Appl. Phys. **40** (2007) 2615–2623 doi:10.1088/0022-3727/40/9/S01

# Photonic crystal defect mode cavity modelling: a phenomenological dimensional reduction approach

**Weidong Zhou, Zexuan Qiang and Li Chen**

Department of Electrical Engineering, Nanofab Center, University of Texas at Arlington, Arlington, TX 76019-0072, USA

E-mail: wzhou@uta.edu

Received 20 July 2006
Published 19 April 2007
Online at stacks.iop.org/JPhysD/40/2615

**Abstract**

A phenomenological dimensional reduction approach (PDRA) for the cavity characteristics in defect mode based photonic crystal (PC) lasers is presented. Based on the fully vectorial three-dimensional finite-difference time-domain (3D FDTD) technique, simultaneous enhancement and suppression in spontaneous emission and absorption were obtained in an absorptive photonic crystal slab (PCS) cavity. Effective index perturbation (EIP) was proposed for fast and accurate determination of the effective index and the dominant resonant cavity frequency in a 3D PCS structure, with two-dimensional (2D) FDTD simulation. Further dimensional reduction from 2D to one-dimensional planar cavity enables phenomenological modelling of lasing characteristics via the effective reflectivity calculation and rate equation analysis. Very fast and accurate results have been achieved with this PDRA approach. A high spontaneous emission factor and cavity quality factor $Q$ were obtained in a single defect cavity, which led to over an order reduction in lasing gain threshold. The model offers a fast and accurate tool for the design and modelling of PC defect mode cavity based devices and aids the research in the proposed novel defect mode based devices such as ultra-compact light sources on Si and spectrally resolved PC infrared photodetectors.

(Some figures in this article are in colour only in the electronic version)

## 1. Introduction

Owing to the ability of photon density manipulation and light-matter interaction alternation, photonic crystals (PCs or PhCs) [1, 2] offer a disruptive platform for nanophotonics, where ultra-compact, high performance light sources, modulators, detectors and sensors can all be realized, potentially on the same chip monolithically integrated [3]. Various device configurations based on PC cavities have been proposed and demonstrated experimentally, mostly based on planar two-dimensional (2D) air hole lattice PC slab (PCS) structures [4–11].

Significant progress has also been made in the computational techniques for the design of PCS based microcavity and in the understanding of these cavity characteristics [12–15]. Works reported to date are mostly based on the three-dimensional (3D) finite-difference time-domain (FDTD) technique. 3D FDTD is a powerful tool to accurately simulate the characteristics of photonic crystal SEL (PCSEL) based on 2D PCS or quasi-3D structure, taking into account the finite thickness in the vertical direction. However, the fully vectorial 3D FDTD approach is extremely time and computer memory consuming.

The effective index method (EIM) [12, 16] has proved to be very effective and efficient/fast in predicting the cavity properties with reduced dimensionality (from 3D to 2D), where only the effective index of fundamental guided mode of the unperturbed slab is considered. EIM is most effective for the low index contrast PCS. However, it becomes less accurate when it is applied to high index contrast PCS, where high

  

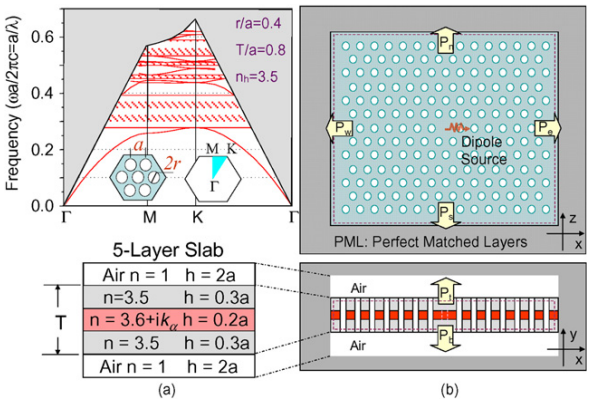


**Figure 1.** (*a*) Photonic dispersion plot for the symmetric air–slab–air PCS, with the thin absorptive layer inserted in the centre of the slab; (*b*) 3D FDTD simulation setup with dipole and monitor locations schematically shown.

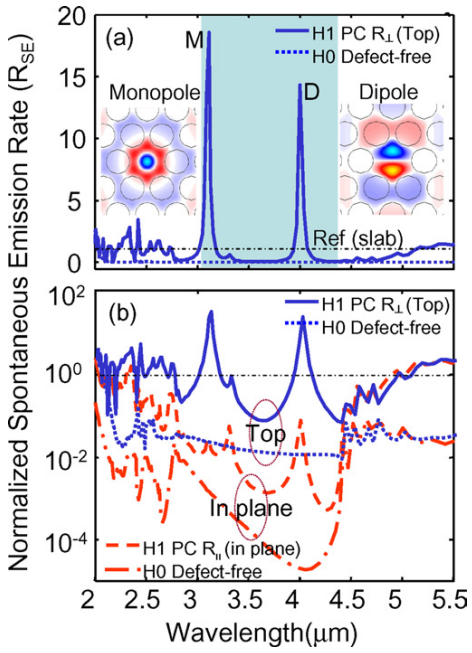


**Figure 2.** (*a*) Linear- and (*b*) log-scale plots of spontaneous emission spectral power density in the lossless (zero absorption) single defect (H1) and defect-free (H0) PCS cavities. The mode profiles for these two defect modes are shown in the inset. The lattice constant $a = 1.22\ \mu$m, with corresponding PBG of 3.1–4.4 $\mu$m. Note the dominant vertical emission as compared with the in-plane transmission.

index contrast is favourable for reduced vertical cavity loss and better mode confinement. Efforts have been reported to adjust the effective index by matching the photonic band diagram (dispersion plot) with frequency offset [17] and effective index modification [18].

In this paper, a phenomenological dimensional reduction approach (PDRA) will be introduced to investigate the gain threshold condition and tradeoffs in cavity design and laser configuration optimization. 3D FDTD simulation results on the spontaneous emission and absorption property modification in a lossy PCS cavity will be given in section 2, followed by the effective index perturbation (EIP) for the dimensional reduction from 3D to 2D FDTD in section 3. Further dimensional reduction from 2D to one-dimensional (1D) will be discussed in section 4, based on the phenomenological approach reported earlier in PC fibres (PCF) [19]. Rate equation analysis [20] results will be discussed in section 5 for the understanding of the gain threshold behaviour in PC laser structures. Conclusions and prospects of defect mode PC cavity based devices will be given in the end.

## 2. 3D FDTD modelling on spontaneous emission and absorption property modulation

Spontaneous emission control and spectrally selective modulation (enhancement and suppression) of emission and absorption properties are highly desirable for advanced photonic devices, including low threshold light sources [9], spectrally selective photodetectors [21, 22], solar cells, etc. Simultaneous inhibition and redistribution of spontaneous emission in PC has been demonstrated theoretically and experimentally in a lossless PCS structure [23]. Following a similar approach, 3D FDTD simulation was carried out in an air–slab–air PC cavity, with an absorptive layer in the centre of the slab, as shown in figure 1. Perfectly matched layers (PMLs) were incorporated at the boundaries of the simulation domain to avoid unnecessary reflection of light at the boundaries. The absorption layer extinction coefficient $k_a$, i.e. the imaginary part of the refractive index, was tuned for different absorption coefficients. A dipole source was introduced in the centre of the cavity, with power monitors placed at the boundaries to collect the transmitted spectral power density after Fourier-transformation for structures with different absorption coefficients. The same calculation was performed for the slab waveguide without PCs as reference. The results were normalized to the results obtained from the reference sample (slab without PC).

Normalized spontaneous emission rates were obtained in single defect and defect-free PC cavities based on the calculation on the lossless PCS (zero absorption). Enhanced spontaneous emission (up to 18 times higher) was obtained at defect mode levels within the photonic bandgap (PBG), as shown in figure 2. At the same time, suppression emission (at least two orders lower) was observed in the PBG region for single defect (H1, other than the defect mode levels) and for defect-free (H0) PC cavities. Based on the simulation, it is further confirmed that the vertical emission power spectral density is a few orders higher than the in plane emission spectral density. It is also worth noting that two different defect modes exit in this simple single defect (H1) cavity, as confirmed by the mode property plots, shown in the inset of figure 2(*a*). Further design optimization can lead to the shift in defect levels for the desired spectral selectivity and even higher spontaneous emission enhancement.

A similar approach has been taken to obtain the absorption power spectral density, based on the transmission spectral power density calculations with different absorption coefficients. Simultaneous enhancement and suppression of absorption were also obtained in single defect PC cavities, with one example shown in figure 3, with the imaginary part

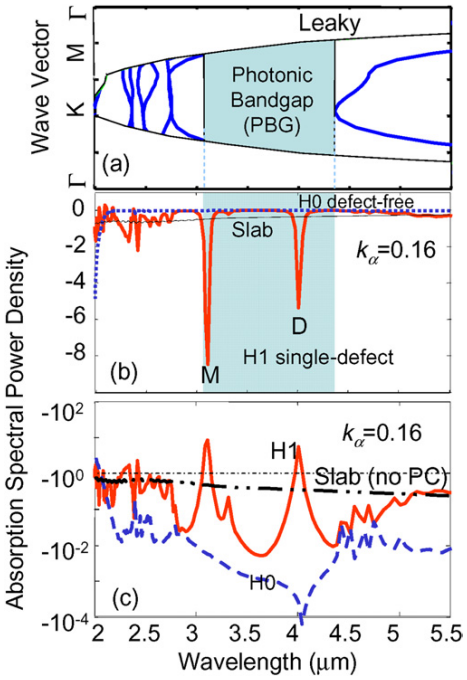


**Figure 3.** (*a*) Photonic band diagram calculated by the PWE technique with $a = 1.22\,\mu$m; (*b*) linear- and (*c*) log-scale plots of absorption power at $ka = 0.16$ for single defect (H1), defect-free (H0) and slab without PC structures.

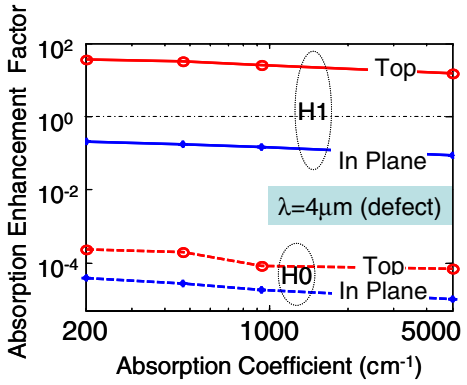


**Figure 4.** Absorption enhancement factors in absorptive PCS defect cavities at the defect level (dipole mode, $\lambda = 4\,\mu$m) for a large range of absorption coefficients.

of the refractive index $k_a = 0.16$ (corresponding to absorption coefficient of $5 \times 10^3$ cm$^{-1}$ at $\lambda = 4\,\mu$m).

The absorption enhancement factor, defined as the relative absorption power spectral density compared with that obtained from the reference slab (without PC) with the same absorption coefficient, can be derived from the normalized absorption power spectral density. The absorption change (absorption enhancement factor) due to the presence of the PC cavity is shown in figure 4, at the defect-level wavelength ($4\,\mu$m), for different absorption coefficients. Enhanced absorption can be obtained with the enhancement factor greater than 36. The high enhancement factor can be obtained for a large range of absorption coefficients. High spectral selectivity is enabled

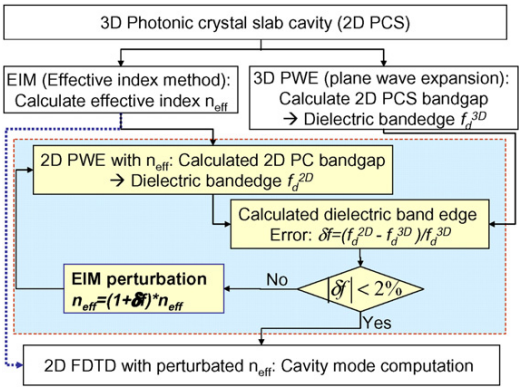


**Figure 5.** Proposed procedure for accurate computation of PC defect-cavity resonant mode location based on EIP. The conventional EIM approach is shown with dashed lines.

due to the spectrally selective enhancement and suppression of absorption. Similar to the spontaneous emission case, the dominant absorption occurs at the surface normal vertical direction ($R\perp$), due to the high in plane cavity $Q$. Further investigation reveals drastically different properties in emission and absorption due to the complicated mode properties in other types of defect cavities, such as multi-defects and coupled cavities (distributed defects).

## 3. From 3D PCS to 2D PC: EIP

We introduced an EIP technique [24] in determining the suitable effective index for the accurate prediction of cavity modal property and defect mode locations based on 2D and 3D plane wave-expansion (PWE) techniques and 2D FDTD method. In donor-like defect mode cavities formed in air-column based PCSs, very good agreement in defect mode locations was obtained with the EIP technique by matching the dielectric band edges simulated from 2D and 3D PWE techniques. The highest $Q$ mode can also be correctly predicted, which is also very important in PC microcavity design, where the mode with the highest cavity $Q$ could be most important in determining the cavity characteristics, including lasing and sensing.

It is well known that the air-band mode is more affected by removing an air hole and finally a donor state is excited and pulled into the bandgap from the air band [25]. In standard EIM, a relatively large error in predicting the resonant mode locations is often seen as a result of the large offset in simulated PBG. This leads us to believe an accurate prediction of resonant peak locations from 2D FDTD is feasible by properly adjusting the effective index to match the simulation PBGs. In this study, we found that suitable perturbation in effective index ($n_{\text{eff}}$) can lead to very small computation errors in resonant peak locations for these donor-like modes by matching the dielectric band edge. The procedure to choose the suitable $n_{\text{eff}}$ is illustrated in figure 5. First, the dielectric band edge of 2D PCS without defect, $f_{\text{d}}^{\text{3D}}$, is calculated by 3D PWE. The standard effective refractive index of unperturbed slab waveguide is also done at this step by conventional methods [26]. Secondly, the 2D PCS is transformed into an ideal 2D PC structure with the high refractive index $n_{\text{h}}$ replaced by the slab effective refractive

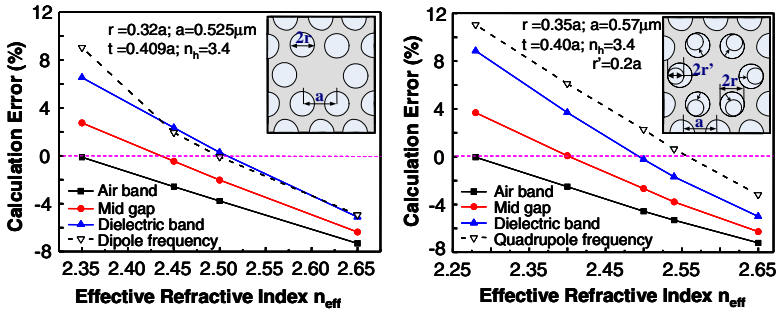


**Figure 6.** Calculation errors for the band gap and resonant frequencies with perturbated effective indexes in two different structures: (*a*) standard single defect cavity reported by Painter *et al* [27]; (*b*) modified single defect cavity reported by Park *et al* [28] where t is the slab thickness.

index $n_{\text{eff}}$. The dielectric band edge of 2D PC without defect, $f_{\text{d}}^{\text{2D}}$, is calculated by 2D PWE. The calculated frequency error is computed as $\delta f = (f_{\text{d}}^{\text{2D}} - f_{\text{d}}^{\text{3D}})/f_{\text{d}}^{\text{3D}}$. If $\delta f$ is greater than 2%, an effective index perturbation is done to adjust the effective index $n_{\text{eff}}$ based on $\delta f$ (with sign): $n_{\text{eff}} = (1+\delta f)\cdot n_{\text{eff}}$. Step 2 is repeated with perturbated $n_{\text{eff}}$ until $\delta f$ is less than 2%. Finally, we use the satisfied $n_{\text{eff}}$ to calculate the quality factor and resonant wavelength by using the 2D FDTD method in 2D PCs with defect. Note that the criterion of 2% is set so that only one or two iterations are needed to get the accurate effective index. Higher accuracy with smaller tolerance could translate into more computation times with more iteration steps. It is also worth noting that in the process of finding proper $n_{\text{eff}}$, the defect-free structure can be used for 3D and 2D PWE based bandgap calculations, which can greatly simplify the supercell construction, and thus reduce the computation time. This is valid in the air-column based PC structures with defect formed by removing/modifying the air hole sizes in the cavity region [25].

2D air–slab–air high index contrast PCS structures with single defect in the centre of the air-column PCs are considered here, as shown in the insets of figure 6. To validate the proposed EIP approach, simulations were done based on the structural parameters reported by Painter *et al* [27] and Park *et al* [28], where both 3D FDTD simulation results as well as experimental results were reported for the effective validation of our approach. In addition to the effective index obtained based on the standard EIM (denoted as case I in figure 7), three additional effective indexes were obtained by matching the PBG obtained from 2D PWE with the PBG obtained from 3D PWE, where matching criteria were set to be the dielectric band edge (case II), middle gap position (case III) and air band edge (case IV), respectively. The calculation errors for the band gap position are calculated based on the 2D and 3D PWE technique with different effective indexes (cases I to IV). Note that a large frequency offset (red-shift in the bandgap centre frequency) is seen with standard EIM. It is mainly due to the fact that the standard EIM approach only considers the slab without PCs, which leads to an overestimate of the effective index since the average index for the real slab is indeed smaller. Perturbation in the effective index (reducing it in this case) should lead to a better match in bandgap position and thus a better match in resonant peaks. 2D FDTD computation was carried out to find the defect mode locations and quality factors. The calculation error for the computed resonant peak locations for different effective indexes is derived by comparing the defect mode frequency simulated from 2D FDTD ($f_r^{\text{2D}}$) to the frequency simulated based on 3D FDTD ($f_r^{\text{3D}}$) with the following formula ($\delta f_r = (f_r^{\text{2D}} - f_r^{\text{3D}})/f_r^{\text{3D}}$). Only the defect mode with the highest $Q$ is shown in figure 6. Note that very good agreement is obtained in the highest $Q$ mode location ($\delta f_r < 2\%$) for case IV, where the effective index is taken such that the calculation error for the dielectric band edge is approaching zero.

In cases where multiple modes exist in the defect cavity, it is very important that the modal property does not change with the perturbation of effective index. Detailed modal property simulations were carried out for the structure shown in figure 6(*b*), where monopole ($M$), dipole ($D$), quadrupole ($Q$), and hexapole ($H$) co-exist. The cavity mode profiles are shown on top of figure 7, with vertical dashed lines marking the corresponding defect mode locations based on 3D FDTD simulations. The normalized $Q$ values for different cavity modes are plotted for four cases I to IV. Based on figure 7, it is seen (dotted lines connecting four different modes for each case) that the relative $Q$ values (normalized to the maximum $Q$ value in each case) remain unchanged for four different modes ($M$, $Q$, $H$, $D$), with quadrupole mode being the highest $Q$ mode for all cases. It can also be seen (dotted lines connecting the same modes in four cases with four different effective indexes) that all the modes within the cavity shift proportionally with respect to the band gap positions. A very good match in the mode location is evident for case II, where defect mode frequencies match the target frequencies simulated from 3D FDTD. In this case II, the effective index is adjusted to have the dielectric band edge matched ($n_{\text{eff}} = 2.54$). It is also worth noting that the adjustment in effective index only changes the defect mode location and the absolute $Q$ values. The absolute $Q$ for the highest $Q$ cavity mode (quadrupole as shown) is shown in the inset, where $Q$ value increases with the increase in effective index.

Further validation is done by varying the radius $r'$ for the structure shown in figure 6(*b*). Calculation errors for the quadrupole mode frequency are within 2% for the perturbated effective index of 2.54 for different $r'/a$ values (see figure 8). Further fine tuning is possible for even more accurate calculation in the resonant peak locations (<1% error), with better matched (dielectric) band edge.

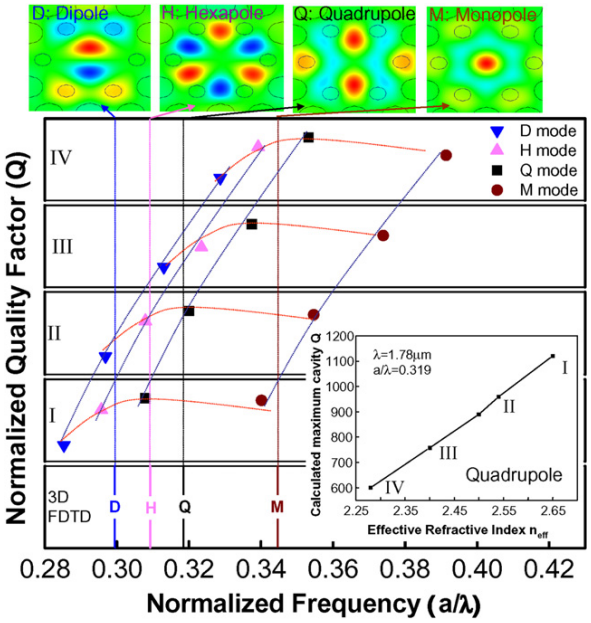


**Figure 7.** Normalized quality factors for four different modes in the modified single defect cavity (figure 2(*b*)) for cases I to IV, where the modal profiles are shown on top of the plot, along with the target frequencies based on 3D FDTD simulation shown as the vertical dotted lines. The perturbated effective indexes are shown in the inset with the absolute cavity $Q$ for the highest cavity $Q$ mode (quadrupole mode in this case). A very good frequency match is seen for the quadrupole mode (the highest cavity $Q$ mode) for case II ($n_{\text{eff}} = 2.54$).

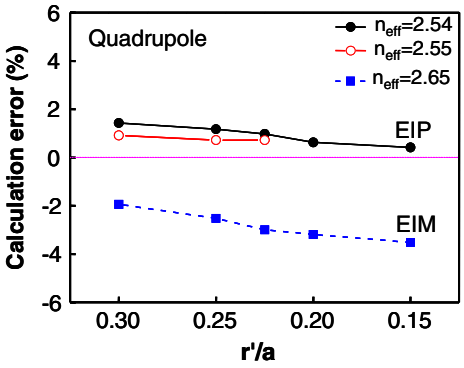


**Figure 8.** Reduced calculation errors are plotted for modified single defect cavity structure shown in figure 2(*b*) with different inner hole radii (r′), based on standard EIM and proposed EIP approaches.

## 4. From 2D PC to 1D planar cavity: transfer matrix method and effective reflectivity

Rate equations have been proven to be a very powerful tool in the semiconductor laser research, for both edge-emitting lasers (EELs) and vertical-cavity surface-emitting lasers (VCSELs) [20]. The gain threshold condition based on the total cavity loss in 1D cavity analysis offers an intuitive and accurate tool for the lasing behaviour study. The lasing mechanism in PC defect mode cavity based lasers differs from that in the conventional laser cavities. While lasing in DBR based *vertical cavity*

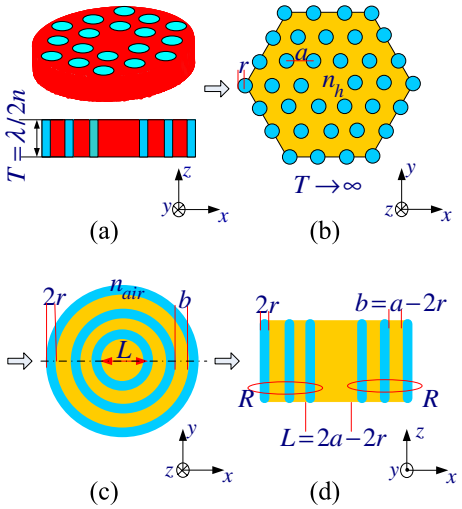


**Figure 9.** PCSEL model simplification process: (*a*) 2D PCS PCSEL structure ($n_{\text{h}}/n_{\text{l}}$) cross-sectional view; (*b*) top view of equivalent ideal 2D PC with $n_{\text{h}} = n_{\text{eff}}$; (*c*) top view of equivalent 1D circular PC structure; (*d*) simplified 1D planar structure cross-sectional view. The relations of the structural parameters are also shown.

surface-emitting lasers (SEL) (VCSEL) is due to the high $Q$ cavity in the vertical direction, lasing in PCSEL is primarily due to the high $Q$ *in plane* microresonator. The vertical confinement is simply based on waveguide and total internal reflection (TIR) principles. Due to its ability of spontaneous emission control, an ultra-small (subwavelength size) high $Q$ microcavity can be formed in a centre of the PC, where the defect is intentionally introduced to create a localized defect mode. Most of the energy of the defect mode leaks vertically, rather than being guided by the slab waveguide.

1D method for the analysis of 2D PC structures has also been investigated in the research of PC fibres [19]. Here we attempt to build a new model for relaxed computational requirement in order to offer phenomenological analysis of the properties of PCSELs, mainly through the dimensional equivalence and reduction. The PCSEL model is illustrated in figure 9. First, the 2D PCS waveguide (3D structure) (figure 9(*a*)) is transformed into an ideal 2D PC structure with the high refractive index $n_{\text{h}}$ replaced by the slab effective refractive index $n_{\text{eff}}$ for a guided slab mode (figure 9(*b*)) [12], based on the EIP technique discussed earlier. Effective index and cavity (lasing) resonance can be determined. Secondly, the ideal 2D PC structure is converted to 1D circular distributed periodic structure, with dimensions defined in the figure (figure 9(*c*)). Finally its 1D equivalent planar waveguide structure (figure 9(*d*)) is obtained by slicing the 1D circular structure through its centre along the dotted line shown in figure 9(*c*). Based on the transfer matrix element method (TMM) [20, 29], we can easily obtain the effective reflectivity $R$, cavity length $L_{\text{eff}}$, total cavity quality factor $Q_{\text{T}}$ and photon lifetime $\tau_{\text{p}}$. This model can then effectively predict the lasing performance of PCSELs, employing the conventional Fabry–Perot cavity theory for the gain threshold condition and spontaneous emission factor calculations [30]. Note that this model cannot reveal the detailed modal properties, which have

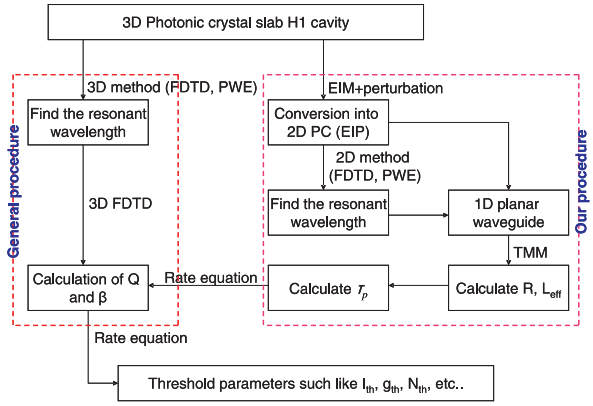


**Figure 10.** Proposed PDRA for the cavity characteristics in defect mode based PC lasers.

to be calculated with 3D computation methods (e.g. FDTD). It is also best suitable for PCSELs with single defect symmetrical configurations.

### *4.1. EIP for the determination of effective index and cavity resonant frequency*

Detailed transmission characteristics were first studied to validate the proposed model, based on the PWE technique and TMM. Nearly identical bandgaps were obtained for the 2D PCS structure ($n_h = 3.4$) and 1D planar structure ($n_{eff} = 2.65$), respectively. All the design parameters are normalized to the lattice constant $a$ of the air hole structure.

Typically the resonant modes of H1 cavity can be calculated with the 3D PWE [31], 3D FDTD [32] and 2D PWE plus the effective refractive index method [28]. Generally, 3D methods occupy lots of time and the PWE method could not calculate the quality factor of cavity. Thus, the 2D FDTD plus the effective refractive perturbation method is considered here. Then quality factor, $Q$, can be calculated by using $Q = \omega_0(t - t_0)/[\ln U(t_0) - \ln U(t)]$ where $\omega_0$ is the resonant frequency, $U(t)$ is the stored electromagnetic energy at time $t$ and $t_0$ is the switch off time of the dipole oscillation (Gaussian frequency profile). It should be mentioned that the quality factor (in plane $Q_\parallel$) calculated by the 2D FDTD method is different from the in plane $Q_\parallel$ obtained by 3D FDTD owing to neglecting the vertical loss. However, it is still useful in determining a suitable configuration to perform high quality factor. Plus, the total cavity $Q_T$ obtained from this approach agrees very well with the values reported, based on the vertical $Q_\perp$ and lateral $Q_\parallel$ calculations in 3D FDTD ($Q_T^{-1} = Q_\perp^{-1} + Q_\parallel^{-1}$). The proposed procedure is outlined in figure 10.

### *4.2. Calculations of the quality factor and spontaneous emission factor*

Once the effective index and the resonant wavelength is set with EIP technique we can easily use TMM to calculate the effective $R$ and $L_{eff}$. From equations (1) and (2), we can obtain the values of the total cavity quality factor $Q_T$ and photon lifetime $\tau_p$.

$$\frac{1}{\tau_p} = v_g(\langle\alpha_i\rangle + \alpha_m) = v_g\left(\langle\alpha_i\rangle + \frac{1}{L_{eff}}\ln\frac{1}{R}\right), \quad (1)$$

$$Q = \omega_0\tau_p = \frac{2\pi c}{\lambda_0}\tau_p, \quad (2)$$

where $c$ is the speed of vacuum, $\lambda_0$ is the resonant wavelength. The spontaneous emission factor or sometimes spontaneous emission coupling efficiency, $\beta$, is defined as the ratio of radiation energy coupled to a lasing mode to the total radiation energy [20]. Two approaches can be used to estimate $\beta$ such as 3D FDTD methods [13] and rate equations [30]. Actually, the spontaneous emission factor is related to carrier density [33] and determined mostly by the shape of the light-current curve below and near threshold [8].

## 5. Rate equation analysis and gain threshold reduction

In general, the carrier density $N$ in the active region $V_a$ and the photon density $N_P$ in the photon cavity $V_P$ can be described by the following rate equations [20]:

$$\frac{dN}{dt} = \eta_{in}\frac{I_a}{qV_a} - \left(\frac{S_a}{V_a}v_s N + BN^2 + CN^3\right) - G(N)N_P, \quad (3)$$

$$\frac{dN_P}{dt} = \Gamma G(N)N_P + \beta BN^2 - \frac{N_P}{\tau_P}, \quad (4)$$

where $I_a$ is the injection current, $q$ is the electron charge, $\eta_{in}$ is the injection efficiency, $v_s$ is the non-radiative velocity, $B$ is bimolecular radiative coefficient, $S_a$ is the surface recombination area, $C$ is the Auger non-radiative recombination coefficient, $\Gamma$ is the confinement factor proportional to the ratio $V_a/V_p$, $\tau_p$ is the photon lifetime and $G(N)$ is the stimulated emission carrier dependent gain and can be expressed with three-parameter model as

$$G(N) = v_g g(N) = \frac{c}{n_{eff}} \cdot \frac{g_0}{1 + \varepsilon N_P}\ln\left(\frac{N + N_s}{N_0 + N_s}\right), \quad (5)$$

where $v_g$ is the group velocity, $g_0$ is the gain coefficient, $\varepsilon$ is the gain compression factor, $N_0$ is the transparent carrier density and $N_s$ is the offset carrier density.

According to the definition of threshold injection current which is defined as the injection current where the photon number inside the optical mode volume is equal to 1 [34, 35], the threshold current and threshold gain can be thus derived from equations (3)–(5) and expressed as

$$I_{th} = \frac{qV_a}{\eta_{in}}\left[BN_{th}^2 + \frac{S_a}{V_a}v_s N_{th} + CN_{th}^3 + \frac{1}{\Gamma}\frac{v_g(\langle\alpha_i\rangle + \frac{1}{L}\ln\frac{1}{R})}{V_P} - \beta(N_{th})BN_{th}^2\right], \quad (6)$$

$$\Gamma g(N_{th}) = \langle\alpha_i\rangle + \frac{1}{L_{eff}}\ln\frac{1}{R} - \frac{\Gamma\beta(N_{th})BN_{th}^2V_P}{v_g}, \quad (7)$$

where $N_{th}$ is the threshold carrier density.

It is worth noting that the simplified 1D structure is not necessarily quarter wavelength distributed Bragg reflector

**Table 1.** Simulation parameters for the modelling.

| Parameters | Symbol | Unit | Value |
|---|---|---|---|
| Wavelength | $\lambda$ | nm | 1550 |
| Transparent carrier density | $N_0$ | $cm^{-3}$ | $1.5 \times 10^{18}$ |
| Offset carrier density | $N_s$ | $cm^{-3}$ | $1 \times 10^{18}$ |
| Gain coefficient | $g_0$ | $cm^{-1}$ | 1700 |
| Gain compression factor | $\varepsilon$ | $cm^3$ | $1.5 \times 10^{-17}$ |
| Surface recombination velocity | $v_s$ | $cm\,s^{-1}$ | $1.2 \times 10^4$ |
| Bimolecular | B | $cm^3\,s^{-1}$ | $1.6 \times 10^{-10}$ |
| Auger | C | $cm^6\,s^{-1}$ | $5.0 \times 10^{-29}$ |
| Internal cavity loss | $\alpha$ | $cm^{-1}$ | 30 |
| Injection efficiency | $\eta_{in}$ | — | 0.75 |
| Extraction efficiency | $\eta_o$ | — | 0.25 |

(DBR). It may not preserve the modal properties in the 2D PCS structure. Nevertheless, it is a simple and effective model to investigate the gain threshold conditions and the trade-offs among various design parameters.

Simulation parameters are given in table 1. Single defect cavity was studied with focus on the impact of number of surrounding air hole period $N_{period}$. The $R$, $L_{eff}$, $Q_T$ and $\tau_p$ are computed based on the TMM method, with calculated total cavity quality factor $Q_T$ and effective reflectivity $R$ shown in figure 11($a$). For simplicity, here we assume a cavity loss of $30\,cm^{-1}$. From figure 11($a$), it is obvious that $Q_T$ and $R$ increase with the increase in surrounding air hole period $N_{period}$ and saturate for $N_{period}$ larger than 6, mainly limited by the vertical $Q_\perp$. This agrees very well with the total cavity $Q_T$ calculated based on the 3D FDTD simulations reported by Painter *et al* [12].

It is worth noting that in our 1D planar cavity modelling, we assume the lasing mode (and corresponding wavelength) is always the one with the highest $Q_T$. The FDTD method was carried out to investigate the correlations between the cavity mode and cavity $Q_T$. As shown in figure 11 two different configurations were calculated, considering different air fill factors ($r/a$) and reduced radius for the first period of surrounding air holes. The total quality factor of the cavity increases as the resonant frequency approaches the centre of the PBG, which could be monopole, dipole or other higher order modes.

Lasing performance was evaluated based on rate equation analysis, based on the 1D planar cavity and effective cavity length, reflectivity and quality factor, based on the TMM method mentioned earlier. The threshold carrier density $N_{th}$ and threshold current $I_{th}$ for single defect PCSEL cavity were obtained. No lasing was observed for $N_{period}$ less than three. As shown in the inset of figure 11($b$), the spontaneous emission factor $\beta$ increases with the increase in $N_{period}$ and saturates for $N_{period}$ larger than 7, owing to the spontaneous emission control. Similar behaviour in the lasing threshold current was observed as well, which agree very well with previously reported data. It is also worth noting that the minimal threshold current of 50 $\mu$A is largely limited by the non-radiative surface recombination current ($I_{nr}$), which can be further reduced to below 10 $\mu$A with efficient electrical injection for minimal $I_{nr}$ [36].

The lasing threshold gain coefficient reduces with the increase in surrounding air hole period $N_{period}$. Minimal gain threshold of $30\,cm^{-1}$ was obtained when $N_{period}$ is larger than 7,

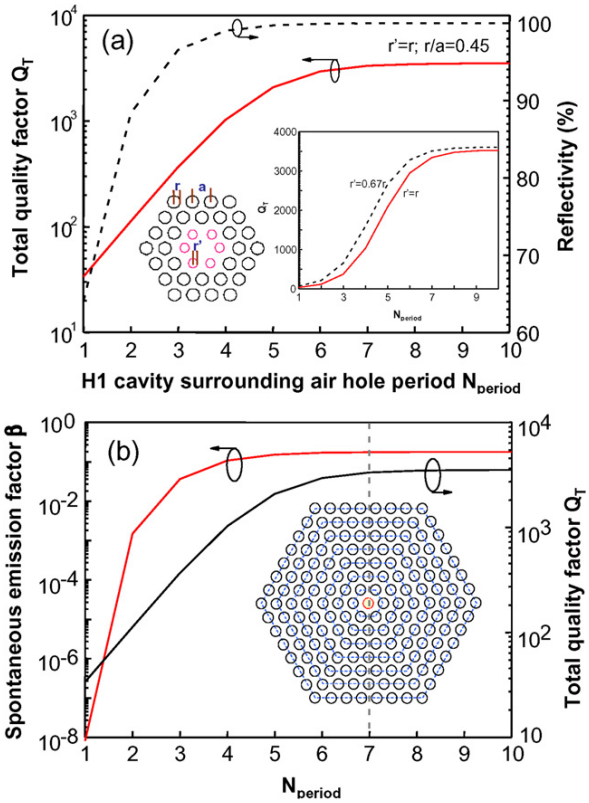


**Figure 11.** Calculated cavity parameter and gain threshold conditions: ($a$) cavity quality factor $Q_T$ and effective reflectivity $R$, with inset showing the $Q_T$ for two different defect configurations; ($b$) spontaneous emission factor $\beta$ and total cavity $Q_T$. Note the optimal period for the surrounding air hole is ∼7.

based on the conventional gain threshold conditions (neglect $\beta$ term in equation (6)). However, in high $Q$ microcavities, where spontaneous emission factor is large, it is necessary to take into account the gain threshold reduction due to increased spontaneous emission rate (equation (6)). It is experimentally proved that the spontaneous emission rate enhancement can be one order higher in these single defect PC cavities [23, 34]. For simplicity, we consider $g_{th}$ without $\beta$ item in this work. Further work will be reported later by taking into account the spontaneous emission rate change through FDTD simulation and Fermi's golden rule analysis.

Owing to the spontaneous emission control, relaxed gain threshold requirement is expected, as shown in figure 12. It is worth noting that the reduction in gain threshold opens a door for novel lasers based on relatively low gain materials, including nanocrystal quantum dot systems. For conventional lasers (EELs and VCSELs), the spontaneous emission factor $\beta$ is in the range $10^{-5}$–$10^{-3}$ (inset of figure 12). Lasing is achieved with relatively high gain III–V materials ($10^3$–$10^4\,cm^{-1}$ for GaAs, InAs, InP, etc). On the other hand, one order lower gain threshold is anticipated in PCSELs, where the spontaneous emission factor $\beta$ can be higher than 0.1. Such a reduction in gain threshold provides an effective means to achieve lasing based on relatively low gain medium with typical gain values of $10^2$–$10^3\,cm^{-1}$.

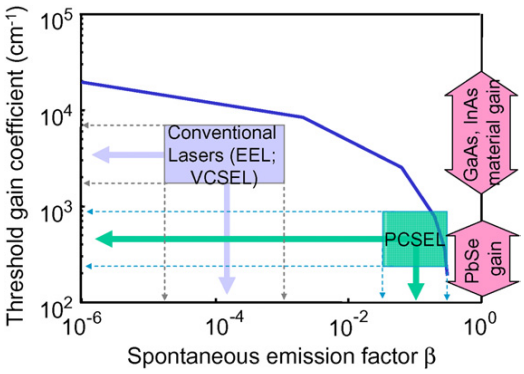


**Figure 12.** Gain threshold conditions for different spontaneous emission factors $\beta$, based on PCSEL simulations. Note the reduction in gain threshold from $10^3$–$10^4$ cm$^{-1}$ in conventional laser cavities to $10^2$–$10^3$ cm$^{-1}$ in PC cavities.

## 6. Conclusions

In summary, a PDRA is proposed to study the defect-cavity characteristics and lasing threshold behaviour in the otherwise complicated 2D PCS structures. Spectrally selective absorption enhancement/suppression was investigated for the first time in defect mode cavities. EIP technique was proposed and validated for accurately correlating the effective index with the PBG and defect mode locations. Based on the derived 1D planar cavity mode with PDRA, the threshold current reduction and relaxed gain threshold were achieved in single defect PCSELs with air hole periods larger than 7. Over one order reduction in lasing gain threshold is demonstrated, making lasing in PC defect cavities feasible with relatively low gain medium. Based on the work reported here, we propose the following devices for research: (1) nanoparticle (e.g. silica) back filled PC cavities for efficient electrical injection. This so-called encapsulated PC structure offers an excellent platform for flexible integration with mechanical stability and for efficient charge injection with optimal contact placement [36]; (2) replacing silica nanoparticle with other functional nanostructures (e.g. colloidal quantum dots), it is feasible to develop high performance light sources (and lasers) on Si. Excellent lasing cavity based defect mode PC cavities can open a promising path towards Si lasers with relative low gain medium (e.g. PbSe colloidal quantum dots), due to the relaxed gain threshold requirement in PC cavities; (3) the incorporation of PCs into infrared (IR) photodetectors (e.g. quantum well and quantum dot infrared photodetectors) can potentially lead to IR photodetectors with higher operation temperature due to enhanced spectrally selective absorption. The spectral resolution and tunability can be accomplished through PC defect engineering.

## Acknowledgments

The authors acknowledge the support from the Air Force Office of Scientific Research (AFOSR) under the SPRING and Nano programs and from the University of Texas Arlington REP program.

## References

[1] Yablonovitch E 1987 Inhibited spontaneous emission in solid-state physics and electronics *Phys. Rev. Lett.* **58** 2059–62
[2] Joannopoulos J D, Meade R D and Winn J N 1995 *Photonic Crystals* (Princeton: Princeton University Press)
[3] Noda S and Baba T 2003 *Roadmap on Photonic Crystals* (Berlin: Springer)
[4] Johnson S G, Shanhui F, Villeneuve P R, Joannopoulos J D and Kolodziejski L A 1999 Guided modes in photonic crystal slabs *Phys. Rev. (Conden. Matter)* B **60** 5751–8
[5] Painter O, Lee R K, Scherer A, Yariv A, O'Brien J D, Dapkus P D and Kim I 1999 Two-dimensional photonic band-gap defect mode laser *Science* **284** 1819–21
[6] Hwang J K, Ryu H Y, Song D S, Han I Y, Park H K, Jang D H and Lee Y H 2000 Continuous room-temperature operation of optically pumped two-dimensional photonic crystal lasers at 1.6 $\mu$m *IEEE Photon. Technol. Lett.* **12** 1295–7
[7] Zhou W D, Sabarinathan J, Kochman B, Berg E, Qasaimeh O, Pang S and Bhattacharya P 2000 Electrically injected single-defect photonic bandgap surface-emitting laser at room temperature *Electron. Lett.* **36** 1541–2
[8] Park H G, Kim S H, Kwon S H, Ju Y G, Yang J K, Baek J H, Kim S B and Lee Y-H 2004 Electrically driven single-cell photonic crystal laser *Science* **305** 1444
[9] Bhattacharya P, Sabarinathan J, Topol'ancik J, Chakravarty S, Yu P-C and Zhou W D 2005 Quantum dot photonic crystal light sources *Proc. IEEE* **93** 1825–38
[10] Zhou W D, Sabarinathan J, Bhattacharya P, Kochman B, Berg E W, Pei-Chen Y and Pang S W 2001 Characteristics of a photonic bandgap single defect microcavity electroluminescent device *IEEE J. Quantum Electron.* **37** 1153–60
[11] Ryu H Y, Notomi M, Kuramoti E and Segawa T 2004 Large spontaneous emission factor (>0.1) in the photonic crystal monopole-mode laser *Appl. Phys. Lett.* **84** 1067–9
[12] Painter O, Vuckovic J and Scherer A 1999 Defect modes of a two dimensional photonic crystal in optical microcavities *J. Opt. Soc. Am.* B **16** 275–85
[13] Vuckovic J, Painter O, Yong X, Yariv A and Scherer A 1999 Finite-difference time-domain calculation of the spontaneous emission coupling factor in optical microcavities *IEEE J. Quantum Electron.* **35** 1168–75
[14] Ryu H Y, Park H G and Lee Y H 2002 Two-dimensional photonic crystal semiconductor lasers: computational design, fabrication, and characterization *IEEE J. Sel. Top. Quantum Electron.* **8** 891
[15] Yokoyama M and Noda S 2005 Finite-difference time-domain simulation of two-dimensional photonic crystal surface-emitting laser *Opt. Express* **13** 2869
[16] Qiu M 2003 Effective index method for heterostructure-slab-waveguide-based two-dimensional photonic crystals *Appl. Phys. Lett.* **81** 1163–5
[17] Witzens J, Loncar M and Scherer A 2002 Self-collimation in planar photonic crystals *IEEE J. Sel. Top. in Quantum Electron.* **8** 1246–57
[18] Yang L, Motohisa J and Fukui T 2005 Suggested procedure for the use of the effective-index method for high-index-contrast photonic crystal slabs *Opt. Eng.* **44** 078002
[19] Abeeluck A K, Litchinitser N, Headley C and Eggelton B 2002 Analysis of spectral characteristics of photonic bandgap waveguides *Opt. Express* **10** 1320–33
[20] Coldren L A and Corzine S W 1995 *Diode Lasers and Photonic Integrated Circuits* (New York: Wiley)
[21] Posani K T, Tripathi V, Annamalai S, Weisse-Bernstein N R, Krishna S, Perahia R, Crisafulli O and Painter O 2006 Nanoscale quantum dot infrared sensors with photonic crystal cavity *Appl. Phys. Lett.* **88** 151104

[22] Chen L, Zhou W D and Brown G J 2006 Spectral selectivity of photonic crystal infrared photodetctors *Optics East* (Boston: SPIE)
[23] Fujita M, Takahashi S, Tanaka Y, Asano T and Noda S 2005 Simultaneous inhibition and redistribution of spontaneous light emission in photonic crystals *Science* **308** 1296–8
[24] Qiang Z and Zhou W D 2006 Fast calculation of cavity-mode characteristics of photonic crystal cavities *IEEE Photon. Technol. Lett.* **18** 1940–2
[25] Ionue K and Ohtaka K 2004 *Photonic Crystals: Physics, Fabrication and Applications* (Berlin: Springer)
[26] Graham T R and Andrew P K 2004 *Silicon Photonics: an Introduction* (New York: Wiley)
[27] Painter O J, Husain A, Scherer A, O'Brien J D, Kim I and Dapkus P D 1999 Room temperature photonic crystal defect lasers at near-infrared wavelengths in InGaAsP *J. Light. Technol.* **17** 2082–8
[28] Park H G, Kwang J K, Huh J, Ryu H Y, Kim S H, Kim J S and Lee Y H 2002 Characterization of modified single-defect two-dimensional photonic crystal lasers *IEEE J. Quantum Electron.* **38** 1353–65
[29] Katsidis C C and Siapkas D I 2002 General transfer-matrix method for optical multilayer systems with coherent, partially coherent, and incoherent interference *Appl. Opt.* **41** 3978–87
[30] Baba T 1997 Photonic crystals and microdisk cavities based on GaInAsP-InP system *IEEE J. Sel. Top. Quantum Electron.* **3** 808
[31] Monat C *et al* 2003 Two-dimensional hexagonal-shaped microcavities formed in a two-dimensional photonic crystal on an InP membrane *J. Appl. Phys.* **93** 23
[32] Huh J, Kwang J K, Ryu H Y and Lee Y H 2002 Nondegenerate monopole mode of single defect two-dimensional triangular photonic band-gap cavity *J. Appl. Phys.* **92** 654
[33] Ram R J 1996 Spontaneous emission factor in post microcavity lasers *IEEE Photon. Technol. Lett.* **8** 599–601
[34] Altug H and Vuckovic J 2004 Two-dimensional coupled photonic crystal resonator arrays *Appl. Phys. Lett.* **84** 161–3
[35] Imamoglu A and Yamamoto Y 1999 *Mesoscopic Quantum Optics* (New York: Wiley)
[36] Zhou W D 2006 Encapsulation for efficient electrical injection of photonic crystal surface emitting lasers *Appl. Phys. Lett.* **88** 051106